

Self-Supervised Pretraining for RGB-D Salient Object Detection

Xiaoqi Zhao,¹ Youwei Pang,¹ Lihe Zhang,^{1*} Huchuan Lu,^{1,2} Xiang Ruan³

¹ Dalian University of Technology, China

² Peng Cheng Laboratory, China

³ Tiwaki Co.,Ltd., Japan

{zxq,lartpang}@mail.dlut.edu.cn, {zhanglihe,lhchuan}@dlut.edu.cn, ruanxiang@tiwaki.com

Abstract

Existing CNNs-Based RGB-D salient object detection (SOD) networks are all required to be pretrained on the ImageNet to learn the hierarchy features which helps provide a good initialization. However, the collection and annotation of large-scale datasets are time-consuming and expensive. In this paper, we utilize self-supervised representation learning (SSL) to design two pretext tasks: the cross-modal auto-encoder and the depth-contour estimation. Our pretext tasks require only a few and unlabeled RGB-D datasets to perform pretraining, which makes the network capture rich semantic contexts and reduce the gap between two modalities, thereby providing an effective initialization for the downstream task. In addition, for the inherent problem of cross-modal fusion in RGB-D SOD, we propose a consistency-difference aggregation (CDA) module that splits a single feature fusion into multi-path fusion to achieve an adequate perception of consistent and differential information. The CDA module is general and suitable for cross-modal and cross-level feature fusion. Extensive experiments on six benchmark datasets show that our self-supervised pretrained model performs favorably against most state-of-the-art methods pretrained on ImageNet. The source code will be publicly available at <https://github.com/Xiaoqi-Zhao-DLUT/SSLSOD>.

Introduction

RGB-D salient object detection (SOD) task aims to utilize the depth map, which contains stable geometric structures and extra contrast cues, to provide important supplemental information for handling complex environments such as low-contrast salient objects that share similar appearances to the background. Benefiting from Microsoft Kinect, Intel RealSense, and some modern smartphones (e.g., Huawei Mate30, iPhone X, and Samsung Galaxy S20), depth information can be conveniently obtained.

With the development of deep convolutional neural networks (CNNs), many CNNs-Based SOD methods (Zhang et al. 2019, 2020b; Li et al. 2021b; Liu, Zhang, and Han 2020; Fan et al. 2020b; Li et al. 2020; Zhang et al. 2020a, 2021b; Sun et al. 2021; Zhao, Zhang, and Lu 2021; Zhao et al. 2021; Li et al. 2021a; Zhao et al. 2020a; Pang et al. 2020b; Ji et al. 2021b; Li et al. 2022; Zhang et al. 2021a;

Pang et al. 2020a) can achieve satisfactory performance. They all are required to be pretrained on the ImageNet (Deng et al. 2009) to learn rich and high-performance visual representations for downstream tasks. However, the ImageNet contains about 1.3 million labeled images covering 1,000 classes while each image is labeled by human workers with one class label. Such expensive labor costs are immeasurable. Recently, Doersch *et al.* (Doersch, Gupta, and Efros 2015), Wang and Gupta (Wang and Gupta 2015) and Agrawal *et al.* (Agrawal, Carreira, and Malik 2015) have explored a novel paradigm for unsupervised learning called self-supervised learning (SSL). The main idea is to exploit different labeling that is freely available besides or within visual data and to use them as intrinsic reward signals to learn general-purpose features. In the learning process, the context has proven to be a powerful source of automatic supervisory signal for learning representations (Ando and Zhang 2005; Okanohara and Tsujii 2007; Collobert and Weston 2008; Mikolov et al. 2013). The SSL needs to design a “pretext” task to learn rich context and then utilizes the pretrained model for some other “downstream” tasks, such as classification, detection, and semantic segmentation. In addition, for the RGB-D SOD task, how to fully integrate the features of two modalities is still an open problem of great concern, just like the cross-level feature fusion. How to better design a general module suitable for feature pairs with multiple complementary relationships is a currently neglected issue.

Two-stream RGB-D SOD networks (Piao et al. 2019; Liu, Zhang, and Han 2020; Fu et al. 2020; Pang et al. 2020a; Jin et al. 2021; Ji et al. 2020) usually load ImageNet-pretrained weights. Their encoders for RGB and depth streams have the same pretraining task, i.e., image classification. Their decoders also have the same task of saliency prediction. This kind of task homogeneousness in both encoder and decoder can greatly reduce the inter-modal gap between the two streams. We know that image classification network often activates the corresponding semantic region in feature maps (e.g., Class Activation Map), while the depth map possibly highlights salient regions. Inspired by this, we firstly design a pretext task of depth estimation, which can promote the RGB encoder to capture localization, boundary and shape information of objects by comparing relative spatial positions at the pixel level. Moreover, the depth map plays

*Corresponding author.

an information filtering and attention role in RGB-D SOD, which is the same as the class activation map in image classification. Secondly, in order to reinforce the cross-modal information interaction, we design another pretext task of reconstructing RGB channels from the depth map. This task requires that the network learns the way to assign the colors for different positions. Due to the limited prior information, this is a very difficult task, which can stimulate the potential of representation learning and drive the depth encoder to capture the cues of shapes and semantic relationships among different objects and fore/backgrounds. The above two pretext tasks actually form a cross-modal auto-encoder, which only needs pairs of RGB and Depth images without any mutual labels.

In the decoder, we design a pretext task of depth-contour estimation. The reason is twofold: (1) Similar prediction tasks help reduce the gap between the modalities. The contour prediction is an analogous process to saliency detection. (2) The depth contour is cleaner than the RGB contour and tends to better depict edge information about salient object/objects, since based on human cognition, salient objects usually have more pronounced depth difference from the background. Moreover, the contour is also an important attribute of salient object. Once the pretext can predict the contour of the salient object well, it simplifies the downstream RGB-D SOD task to predict fore/background properties inside and outside the contour. After these pretext networks have been trained, the RGB-D SOD network can gain good initialization.

About the network architecture, we propose a general module called consistency-difference aggregation (CDA) to achieve both cross-modal and cross-level fusion. Specifically, for two types of features with complementary relationships, we calculate their jointly consistent (JC) features and jointly differential (JD) features. The JC maintains more attention to their consistency and suppresses the interference of non-salient information, while the JD depicts their difference in salient region and encourages the cross-modal or cross-level alignment. By saliency guided consistency-difference aggregation, the gap between modalities or levels is greatly narrowed. Our main contributions can be summarized as follows:

- We present a self-supervised network closely related to the RGB-D SOD task, which consists of a cross-modal auto-encoder and a depth-contour estimation decoder. It is the first method to use self-supervised representation learning for RGB-D SOD.
- We design a simple yet effective consistency-difference aggregation structure that is suitable for both cross-level and cross-modal feature integration.
- We use 6,392 pairs of RGB-Depth images (without manual annotations) to pretrain the model instead of using ImageNet (1,280,000 with image-level labels). Our model still performs much better than most competitors on six RGB-D SOD datasets.

Related Work

RGB-D Salient Object Detection

Generally speaking, the depth map can be utilized in three ways: early fusion (Peng et al. 2014; Song et al. 2017; Zhao et al. 2020b), middle fusion (Feng et al. 2016) and late fusion (Fan, Liu, and Sun 2014). According to the number of encoding streams, RGB-D SOD methods can divided into two-stream (Zhao et al. 2019; Chen and Fu 2020; Fan et al. 2020b; Liu, Zhang, and Han 2020; Zhang et al. 2020a, 2021b; Sun et al. 2021; Ji et al. 2021a) and single-stream (Zhao et al. 2020b) ones. The two-stream networks mainly focus on sufficiently incorporating cross-modal complementarity. Liu *et al.* (Liu, Zhang, and Han 2020) utilize the self-attention and the other modality’s attention in the Non-local structure to fuse multi-modal information. Chen and Fu (Chen and Fu 2020) propose an alternate refinement strategy and combine a guided residual block to generate both refined feature and refined prediction. Sun *et al.* (Sun et al. 2021) design a new NAS-based model for the heterogeneous feature fusion in RGB-D SOD. These two-stream designs significantly increase the number of parameters in the network. Recently, Zhao *et al.* (Zhao et al. 2020b) combine depth map and RGB image from starting to build a real single-stream network to take advantage of the potential contrast information provided by the depth map, which provides a new perspective on the RGB-D SOD field. Besides, different level features have different characteristics. High-level ones have more semantic information which helps localize the objects, while low-level ones have more detailed information which can capture the subtle structures of objects. However, both two-stream and single-stream networks belittle the cross-level fusion, which may lead to a significant reduction in the effectiveness of the cross-modal fusion. In this work, we propose a consistency-difference aggregation module, which can be applied in universal combination of multiple complementary relationships (RGB/Depth, High/Low level).

Self-Supervised Representation Learning

Self-supervised learning (SSL) is an important branch of unsupervised learning technique. It refers to the learning paradigm in which ConvNets are explicitly trained with automatically generated labels. During the training phase, a predefined pretext task is designed for ConvNets, and the pseudo labels in the pretext task are automatically generated based on some attributes of data. Then the ConvNet is trained to learn object functions of the pretext task. After the SSL training is finished, the learned weights are transferred to downstream tasks as their pretrained models. This strategy can overcome overfitting of small sample problem and obtain the generalization capability of ConvNets.

Many pretext tasks have been designed and applied for self-supervised learning, such as image inpainting (Pathak et al. 2016), clustering (Caron et al. 2018), image colorization (Larsson, Maire, and Shakhnarovich 2017), temporal order verification (Misra, Zitnick, and Hebert 2016) and visual audio correspondence verification (Korbar, Tran, and Torresani 2018). Effective pretext tasks can promote Con-

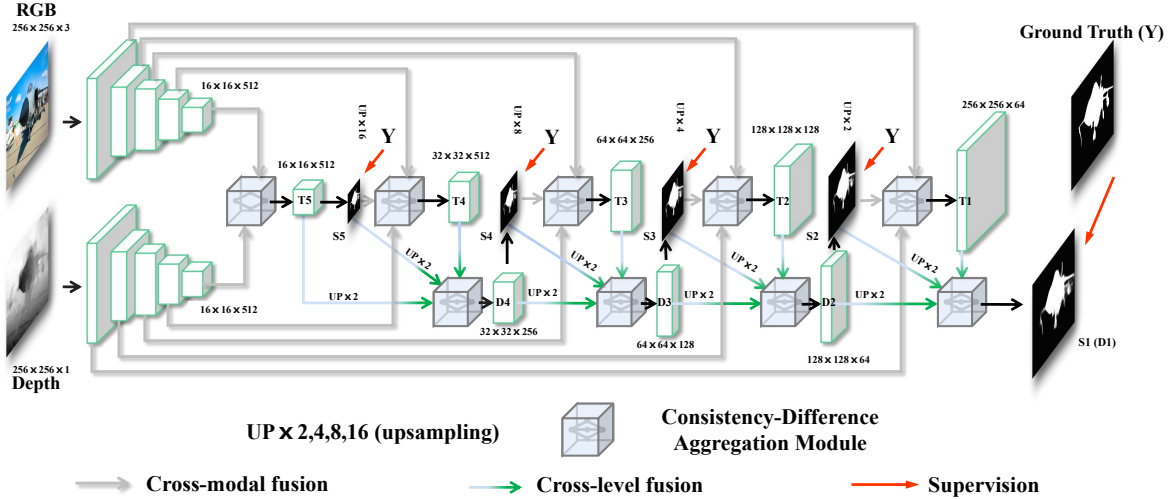


Figure 1: Network pipeline of the downstream task. It consists of two VGG-16 encoders, five cross-modal layers and four decoder blocks. Both the cross-modal and cross-level fusions are achieved by the consistency-difference aggregation (CDA) module. We generate ground truth of multiple resolutions and use cross-entropy loss as supervision.

vNets to learn useful semantic features for the downstream task. In this work, we rely on the characteristics of RGB-D SOD task to design two related pretext tasks: cross-modal auto-encoder and depth-contour estimation. The former encourages the two-stream encoder to learn each modal information and reduce the inter-modal gap. The latter can further facilitate the cross-modal fusion, which also provides a good feature prior to ease the capture of object-contour and object-localization.

The Proposed Method

In this section, we first describe the overall architecture of the proposed RGB-D SOD network. And then, we present the details of the consistency-difference aggregation (CDA) module for cross-modal and cross-level feature fusion. Next, we introduce the designed pretext tasks: cross-modal auto-encoder and depth-contour estimation. Finally, we list all the supervisions and loss functions used in the network for both the pretext tasks and the downstream task.

The Overall Architecture

Our network architecture, shown in Fig. 1, follows a two-stream model that consists of five encoder blocks, five transition layers (T^i $i \in \{1, 2, 3, 4, 5\}$), four decoder blocks (D^i $i \in \{1, 2, 3, 4\}$) and nine consistency-difference aggregation modules. The encoder-decoder architecture is based on the FPN (Lin et al. 2017). The encoder is based on a common backbone network, e.g., VGG-16 (Simonyan and Zisserman 2014), to perform feature extraction on RGB and Depth, respectively. We cast away all the fully-connected layers and the last pooling layer of the VGG-16 to modify it into a fully convolutional network. We convey the output features from the encoding blocks of two modalities to the consistency-difference aggregation module to achieve cross-modal fusion at each level. And the CDA is also embedded in the decoder. Once these cross-modal fused features are obtained, they will participate in the decoder and gradually

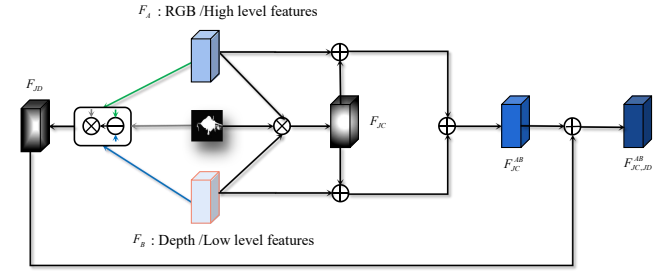


Figure 2: Illustration of the consistency-difference aggregation module.

integrate the details from high-level to low-level, thereby continuously restoring the full-resolution saliency map.

Consistency-Difference Aggregation Module

The consistency-difference aggregation module can strengthen the consistency of features and highlight their differences, thereby increasing inter-class difference and reducing intra-class difference. Fig. 2 shows the internal structure of the proposed CDA module. We use F_A and F_B to represent different modality or level feature maps. They all have been activated by the ReLU operation. First, we use element-wise multiplication between F_A and F_B at the same time constrained by saliency map S of the side-out prediction to obtain high-confidence region features, which are usually consistent with salient objects. This process can be formulated as follows:

$$F_{JC} = Conv(F_A \otimes F_B \otimes S), \quad (1)$$

where \otimes is the element-wise multiplication and $Conv(\cdot)$ denotes the convolution layer. Next, the jointly consistent features are applied to enhance saliency cues in F_A and F_B , thereby yielding initial fused features,

$$F_{JC}^{AB} = Conv(Conv(F_{JC} \oplus F_A) \oplus Conv(F_{JC} \oplus F_B)), \quad (2)$$

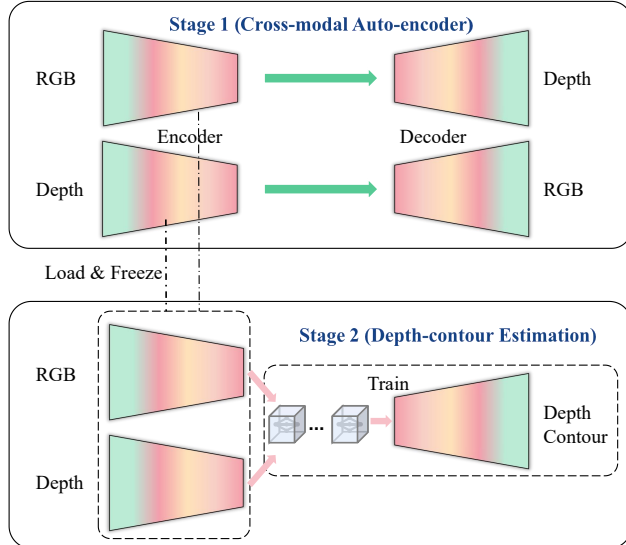


Figure 3: Network pipeline of the pretext tasks. Stage 1: Cross-modal auto-encoder. Stage 2: Depth-contour estimation. The network in Stage 2 is equipped with the CDAs.

where \oplus is the element-wise addition. F_{JC}^{AB} achieves consistency boosting of features, especially in salient regions. We calculate the jointly differential features of F_A and F_B :

$$F_{JD} = \text{Conv}(|F_A \ominus F_B| \otimes S), \quad (3)$$

where \ominus is the element-wise subtraction and $|\cdot|$ calculates the absolute value. F_{JD} depicts the feature difference in salient regions. The final fusion are generated by combining F_{JC}^{AB} and F_{JD} :

$$F_{JC,JD}^{AB} = \text{Conv}(F_{JC}^{AB} \oplus F_{JD}). \quad (4)$$

Compared with F_{JC}^{AB} , $F_{JC,JD}^{AB}$ contains richer complementary information about salient objects. Through a series of addition and subtraction, the features are well aligned under the constraint of the side-out prediction, thereby progressively promoting the correspondence between feature distribution and fore/background categories in the common space, as shown in Fig. 5.

Pretext Tasks: Cross-modal Auto-encoder and Depth-contour Estimation

Instead of previous approaches which obtain effective initial representations through ImageNet pretraining, we design a pure self-supervised network to mine RGB-D information without manual annotations. Fig. 3 shows the structure of the proposed SSL network, which consists of two components, namely, the cross-modal auto-encoder and the depth-contour estimation decoder.

In the first stage, we use pairs of RGB-Depth data to predict each other, i.e., using the RGB image to predict the depth map and using the depth map to reconstruct the RGB image. The backbone of these two networks is based on VGG-16 with random initialization. We directly adopt the FPN as the basic structure. Through the cross-modal auto-encoder, the encoder of the RGB or depth stream can respectively turn to capture the information of another modal.

As a result, the features of the two encoders tend to converge into a common space, which greatly reduces the gap between modalities to facilitate subsequent cross-modal fusion. Moreover, in the process of predicting each other, the contextual representation capabilities can be effectively learned in their own streams. As suggested in (Goyal et al. 2019), increasing the complexity of the pretext task is generally beneficial to the performance of the SSL. In this work, our cross-modal encoders do not interact with each other in any way. The completely independent cross-modal generation obviously elevates the difficulty, making the network try its best to learn useful semantic cues about the two modalities.

In the second stage, we load the parameters of the encoders trained in the first stage to calculate multi-scale features in each encoding stream. And then, we exploit the designed CDA module described in Sec. to achieve the cross-modal and cross-level fusion for predicting the depth-contour. This pretext task allows further cross-modal integration, and the learned features provide contour prior (i.e., a kind of fore/background semantic guidance) for the downstream task to predict saliency map.

Supervision

In our RGB-D SOD network, the total loss is written as:

$$L_{sod} = \sum_{n=1}^N (l_{bce}^w(n) + l_{iou}^w(n)), \quad (5)$$

where l_{bce}^w and l_{iou}^w represent the weighted IoU loss and binary cross entropy (BCE) loss which have been widely adopted in segmentation tasks. We use the same definitions as in (Wei, Wang, and Huang 2020; Fan et al. 2020a; Zhao, Zhang, and Lu 2021). N denotes the number of the side-out. Our RGB-D SOD model is deeply supervised with five outputs, i.e. $N = 5$.

The cross-modal auto-encoder task consists of depth estimation and RGB reconstruction. Since both RGB and depth information presents patch consistency in a scene, we follow the related depth estimation works (Pillai, Ambrus, and Gaidon 2019; Ranftl et al. 2020; Ocal and Mustafa 2020) to adopt the combination loss of the L1 and SSIM (Wang, Simoncelli, and Bovik 2003). The use of SSIM is well suited as a loss function for the patch-level regularization. The L1-loss calculates the absolute distance between the predicted map and ground truth, which is supervised at the pixel-level. The combination of SSIM-loss and L1-loss allows the network to have both patch-level and pixel-level supervision, thereby promoting more locally consistent prediction.

For the depth-contour estimation task, its ground truth (G_{dc}) is calculated based on the depth map (G_d) provided by the RGB-D datasets. Specifically, we employ the morphological dilation and erosion as follows:

$$G_{dc} = D_m(G_d) - E_m(G_d), \quad (6)$$

where $D(\cdot)$ and $E(\cdot)$ are the dilation and erosion operations, respectively. m denotes a full one filter of size $m \times m$ for erosion and expansion. It is set to 5 in this paper. We only use the L1-loss for each side-out during the training phase.

Experiments

Datasets

We evaluate the proposed model on six public RGB-D SOD datasets which are *RGBD135* (Cheng et al. 2014), *DUT-RGBD* (Piao et al. 2019), *STERE* (Niu et al. 2012), *NLPR* (Peng et al. 2014), *NJUD* (Ju et al. 2014) and *SIP* (Fan et al. 2019). For the downstream task, we adopt the same training set as most methods (Piao et al. 2020b; Zhao et al. 2020b; Li et al. 2020), that is, 800 samples from the DUT-RGBD, 1,485 samples from the NJUD and 700 samples from the NLPR are used for training. The remaining images and other three datasets are used for testing. For the pretext tasks, we combine training subsets of NJUD and NLPR with the recent DUTLF-V2 (Piao et al. 2020a) (4, 207 samples) to finish pretraining, that is, 6,392 images in total.

Evaluation Metrics

We adopt several widely used metrics for quantitative evaluation: F-measure (F_{β}^{max}) (Achanta et al. 2009), the weighted F-measure (F_{β}^w) (Margolin, Zelnik-Manor, and Tal 2014), mean absolute error (MAE, \mathcal{M}), the recently released S-measure (S_m) (Fan et al. 2017) and E-measure (E_m) (Fan et al. 2018) scores. The lower value is better for the MAE and the higher is better for others. Generally speaking, large-scale datasets can ensure the evaluation stability of model performance, while small-scale datasets often present large performance fluctuation. Ave-Metric has been used in HDFNet (Pang et al. 2020a) to consider the scale of the data for comprehensive evaluation.

Implementation Details

We first use random initialization to train the SSL cross-modal auto-encoder. And then the parameters of the encoder of each stream are loaded for the following depth-contour estimation. In this process, the parameters of the two-stream encoder are frozen, we only train the decoder with the CDA modules. Once the pretext tasks are finished, we load their parameters to initialize the network for the downstream task (RGB-D SOD).

Our models are implemented based on the Pytorch and trained on a RTX 2080Ti GPU for 50 epochs with mini-batch size 4. We adopt some data augmentation techniques to avoid overfitting: random horizontally flipping, random rotate, random brightness, saturation and contrast. For the optimizer, we use the stochastic gradient descent (SGD) with a momentum of 0.9 and a weight decay of 0.0005. For the pretext tasks, the learning rate is set to 0.001 and later use the “poly” policy (Liu, Rabinovich, and Berg 2015) with the power of 0.9 as a means of adjustment. For the downstream task, maximum learning rate is set to 0.005 for backbone and 0.05 for other parts. Warm-up and linear decay strategies are used to adjust the learning rate.

Comparisons with State-of-the-art

For fair comparisons, the proposed algorithm is compared with 16 state-of-the-art methods that have released codes, including DisenFuse (Chen et al. 2020), A2DELE (Piao et al. 2020b), ICNet (Li, Liu, and Ling 2020), S2MA (Liu, Zhang,

and Han 2020), DANet (Zhao et al. 2020b), CMWNet (Li et al. 2020), BBSNet (Fan et al. 2020b), CoNet (Ji et al. 2020), UCNet (Zhang et al. 2020a), PGAR (Chen and Fu 2020), HDFNet (Pang et al. 2020a), CDNNet (Jin et al. 2021), DFMNet (Zhang et al. 2021b), DSA2F (Sun et al. 2021), DCF (Ji et al. 2021a) and HAINet (Li et al. 2021a). Saliency maps of these competitors are directly provided by their respective authors or computed by their released codes.

Quantitative Evaluation. Tab. 1 shows performance comparisons in terms of the F-measure, weighted F-measure, S-measure, E-measure and MAE scores. According to the proportion of each testing set to all testing sets, the results on all datasets are weighted and summed to obtain an overall performance evaluation, which is listed in the row “Ave-Metric”.

It can be seen that our fully-supervised (i.e., ImageNet pretrained) model ranks first among 18 models in the overall ranking. Among 30 scores of all datasets, our 26 scores reach the top-3 performance. It shows that our model has excellent comprehensive ability. Notably, our self-supervised model still can outperform most fully-supervised methods and ranks ninth among them, which shows the great potential of self-supervised learning and the effectiveness of the pretext tasks we design.

Qualitative Evaluation. Fig. 4 illustrates the visual comparison with other RGB-D SOD approaches. The proposed method yields the results closer to the ground truth in various challenging scenarios. For the images with a single object, our method can completely segment the whole object, while other competitors lose more or less parts of the object (see the 1st and 2nd rows). For images having multiple objects, our method can still accurately localize and capture all the objects (see the 3rd and 4th rows). Moreover, it can be seen that our SSL model even has better visual results compared to other fully supervised methods.

Ablation Study

In this section, we detail the contribution of each component to the overall network. We first verify the effectiveness of the CDA module when the RGB-D SOD networks are pre-trained on the ImageNet. Next, we evaluate the SSL pretext networks by loading different pretrained parameters to the RGB-D SOD network, the performance gain illustrates the benefits of the proposed SSL pretexts. All ablation experiments are based on the VGG-16 backbone.

Effectiveness of Consistency-Difference Aggregation. In Tab. 2, we show the performance contributed by different structures on all RGB-D SOD datasets in terms of the weighted average metrics “Ave-Metric”. The baseline (Model 1) is a two-stream FPN structure with deep supervision. We can see that this baseline has been able to suppress the A2DELE and DisenFuse. Based on this strong baseline, the performance gain is more convincing. Model 2 vs. Model 1 and Model 4 vs. Model 1 show the effectiveness of the jointly consistent features (JC) in cross-modal and cross-level integration, respectively. The JC can significantly improve the performance. Similarly, Model 3 vs. Model 2 and Model 5 vs. Model 4 show the advantages of the jointly differential features (JD). Model 6 is equipped

Metric	Fully-supervised (Pretrained on the ImageNet)																		Self-supervised Ours VGG-16
	DisenFuse ₂₀ VGG-16	A2DELE ₂₀ VGG-16	ICNet ₂₀ VGG-16	S2MA ₂₀ VGG-16	DANet ₂₀ VGG-16	CMWNet ₂₀ VGG-16	BBSNet ₂₀ ResNet-101	CoNet ₂₀ VGG-16	UCNet ₂₀ VGG-16	PGAR ₂₀ VGG-16	HDFNet ₂₀ VGG-16	CDNet ₂₁ VGG-16	DFMNet ₂₁ MobileNet-V2	DSA2F ₂₁ VGG-16	DCF ₂₁ ResNet-18	HAINet ₂₁ VGG-16	Ours VGG-16		
<i>RGBD135</i>	F_{β}^{max} \uparrow 0.877	0.897	0.925	0.944	0.916	0.939	0.923	0.915	0.936	0.926	0.934	0.939	0.930	0.930	0.926	0.936	0.944	0.941	
	F_{β}^w \uparrow 0.779	0.836	0.867	0.892	0.848	0.888	0.845	0.849	0.908	0.855	0.902	0.894	0.888	0.882	0.876	0.898	0.917	0.910	
	S_m \uparrow 0.779	0.886	0.920	0.941	0.905	0.934	0.908	0.909	0.934	0.913	0.932	0.936	0.931	0.916	0.916	0.929	0.936	0.932	
	E_m \uparrow 0.923	0.920	0.959	0.974	0.961	0.967	0.941	0.945	0.974	0.939	0.973	0.969	0.971	0.955	0.958	0.967	0.978	0.976	
	M \downarrow 0.040	0.029	0.027	0.021	0.028	0.022	0.028	0.019	0.026	0.020	0.020	0.021	0.023	0.023	0.019	0.017	0.019		
<i>DUT-RGBD</i>	F_{β}^{max} \uparrow 0.807	0.907	0.875	0.909	0.911	0.905	-	0.935	-	0.938	0.926	0.901	-	0.938	0.941	0.932	0.947	0.930	
	F_{β}^w \uparrow 0.691	0.864	0.784	0.862	0.847	0.831	-	0.891	-	0.889	0.865	0.838	-	0.908	0.909	0.883	0.914	0.883	
	S_m \uparrow 0.798	0.886	0.852	0.903	0.889	0.887	-	0.919	-	0.920	0.905	0.886	-	0.921	0.924	0.909	0.929	0.908	
	E_m \uparrow 0.854	0.929	0.901	0.921	0.929	0.922	-	0.952	-	0.950	0.938	0.917	-	0.956	0.957	0.939	0.958	0.943	
	M \downarrow 0.104	0.043	0.072	0.044	0.047	0.056	-	0.033	-	0.035	0.040	0.051	-	0.031	0.030	0.038	0.029	0.038	
<i>STERE</i>	F_{β}^{max} \uparrow 0.887	0.892	0.897	0.895	0.897	0.911	0.901	0.909	0.908	0.911	0.918	0.909	0.902	0.910	0.915	0.919	0.914	0.897	
	F_{β}^w \uparrow 0.811	0.846	0.815	0.825	0.830	0.847	0.838	0.866	0.867	0.856	0.863	0.855	0.841	0.869	0.873	0.871	0.870	0.845	
	S_m \uparrow 0.883	0.878	0.891	0.890	0.892	0.905	0.896	0.905	0.903	0.907	0.906	0.903	0.898	0.897	0.905	0.909	0.904	0.885	
	E_m \uparrow 0.915	0.928	0.911	0.926	0.927	0.930	0.928	0.941	0.942	0.937	0.938	0.931	0.942	0.943	0.938	0.939	0.929		
	M \downarrow 0.054	0.045	0.054	0.051	0.048	0.043	0.046	0.037	0.039	0.041	0.045	0.039	0.037	0.038	0.039	0.047			
<i>NLPR</i>	F_{β}^{max} \uparrow 0.895	0.898	0.919	0.910	0.908	0.913	0.921	0.898	0.916	0.925	0.917	0.925	0.916	0.916	0.917	0.917	0.923	0.912	
	F_{β}^w \uparrow 0.828	0.857	0.864	0.852	0.850	0.856	0.871	0.842	0.878	0.881	0.869	0.882	0.869	0.881	0.886	0.881	0.889	0.871	
	S_m \uparrow 0.900	0.898	0.922	0.915	0.908	0.917	0.923	0.908	0.920	0.930	0.916	0.930	0.923	0.918	0.921	0.921	0.922	0.913	
	E_m \uparrow 0.933	0.945	0.945	0.942	0.945	0.941	0.948	0.934	0.955	0.955	0.948	0.954	0.951	0.952	0.956	0.952	0.960	0.947	
	M \downarrow 0.035	0.029	0.028	0.030	0.031	0.029	0.026	0.031	0.025	0.024	0.027	0.024	0.026	0.024	0.023	0.025	0.027		
<i>MUD</i>	F_{β}^{max} \uparrow 0.897	0.890	0.903	0.899	0.905	0.913	0.926	0.902	0.908	0.918	0.924	0.919	0.918	0.917	0.917	0.920	0.923	0.913	
	F_{β}^w \uparrow 0.831	0.843	0.833	0.842	0.853	0.857	0.878	0.850	0.868	0.872	0.881	0.878	0.868	0.883	0.878	0.879	0.884	0.872	
	S_m \uparrow 0.889	0.871	0.895	0.894	0.897	0.903	0.916	0.895	0.897	0.909	0.911	0.913	0.906	0.904	0.903	0.909	0.909	0.901	
	E_m \uparrow 0.914	0.916	0.901	0.917	0.926	0.923	0.937	0.924	0.934	0.935	0.934	0.934	0.937	0.941	0.931	0.939	0.932		
	M \downarrow 0.052	0.047	0.051	0.053	0.046	0.046	0.039	0.046	0.043	0.037	0.038	0.042	0.039	0.038	0.042	0.038	0.042		
<i>SP</i>	F_{β}^{max} \uparrow 0.866	0.855	0.882	0.891	0.901	0.890	0.892	0.883	0.896	0.893	0.904	0.888	0.904	0.891	0.900	0.916	0.909	0.895	
	F_{β}^w \uparrow 0.780	0.780	0.793	0.819	0.829	0.811	0.820	0.803	0.836	0.822	0.835	0.812	0.835	0.829	0.841	0.854	0.855	0.830	
	S_m \uparrow 0.859	0.828	0.864	0.872	0.878	0.867	0.874	0.858	0.875	0.876	0.878	0.862	0.883	0.862	0.873	0.886	0.888	0.868	
	E_m \uparrow 0.899	0.890	0.903	0.913	0.917	0.909	0.912	0.909	0.918	0.912	0.921	0.905	0.923	0.911	0.921	0.925	0.927	0.910	
	M \downarrow 0.068	0.070	0.063	0.057	0.054	0.062	0.056	0.063	0.051	0.055	0.050	0.060	0.051	0.057	0.052	0.048	0.046	0.058	
<i>Top 3</i>		0/30	0/30	1/30	3/30	0/30	2/30	5/25	2/30	8/25	6/30	10/30	10/30	4/25	10/30	15/30	12/30	26/30	4/30
<i>Ave-Metric</i>		0.873	0.884	0.894	0.900	0.903	0.906	0.906	0.903	0.906	0.912	0.916	0.906	0.908	0.910	0.915	0.920	0.920	0.906
F_{β}^{max} \uparrow		0.791	0.830	0.815	0.835	0.838	0.839	0.843	0.846	0.860	0.855	0.860	0.848	0.849	0.866	0.870	0.871	0.877	0.855
F_{β}^w \uparrow		0.864	0.866	0.883	0.892	0.891	0.894	0.896	0.892	0.902	0.901	0.905	0.895	0.894	0.900	0.905	0.906	0.906	0.890
S_m \uparrow		0.905	0.917	0.911	0.924	0.927	0.924	0.927	0.930	0.936	0.934	0.929	0.933	0.935	0.940	0.936	0.941	0.929	
E_m \uparrow		0.062	0.050	0.055	0.049	0.047	0.048	0.045	0.044	0.041	0.042	0.040	0.044	0.043	0.041	0.039	0.039	0.037	0.045
<i>Ave - Rank</i>		18	17	16	15	14	13	12	11	7	6	4	10	8	5	3	2	1	9

Table 1: Quantitative comparison of different RGB-D SOD methods. \uparrow and \downarrow indicate that the larger scores and the smaller ones are better, respectively. The best three scores are highlighted in **bold**. The subscript in each model name is the publication year. The corresponding used backbone network is listed below each model name.

No.	B_i	+ CM _{jc}	+ CM _{jd}	+ CL _{jc}	+ CL _{jd}	F_{β}^{max}	F_{β}^w	S_m	E_m	M	Params (MB)
Model 1	✓					0.893	0.829	0.868	0.904	0.050	36.50
Model 2	✓	✓				0.903	0.846	0.883	0.921	0.045	47.50
Model 3	✓	✓	✓			0.908	0.854	0.891	0.927	0.042	58.49
Model 4	✓			✓		0.907	0.854	0.888	0.926	0.042	45.91
Model 5	✓				✓	0.910	0.861	0.894	0.931	0.040	52.18
Model 6	✓	✓	✓	✓	✓	0.920	0.877	0.906	0.941	0.037	74.17
Model 7	✓					0.893	0.829	0.869	0.905	0.050	78.15

Table 2: Ablation experiments of the CDA module. B_i : Baseline with the ImageNet-pretrained backbone. + CM_{jc} and + CM_{jd}: Using the joint consistency features in the cross-modal and cross-level fusion, respectively. + CL_{jc} and + CL_{jd}: Using the joint difference features in the cross-modal and cross-level fusion, respectively. with the CDA module in both the cross-modal and cross-level fusion. Model 6 vs. Model 3 and Model 6 vs. Model 5 demonstrate the generalization of the CDA in the two kinds of information fusion, which complement each other without repulsion. To further evaluate the rationality of this module, the CDA is replaced with some operations of addition and convolution and a similar number of parameters are preserved. This new network is noted as Model 7. Compared to it, Model 6 has obvious advantages on performance.

We visualize intermediate features in the CDA module as shown in Fig. 5. By explicitly superposing the influence of the cross-modal (or cross-level) joint consistency F_{JC} and joint difference F_{JD} under the constraint of saliency map, the fused feature $F_{JC,JD}^{RGB,D}$ (or $F_{JC,JD}^{4,3}$) can highlight salient

No.	B_r	+ P1	+ P2	+ CM	+ CL	F_{β}^{max}	F_{β}^w	S_m	E_m	M

<tbl_r cells="11" ix="3" maxcspan="

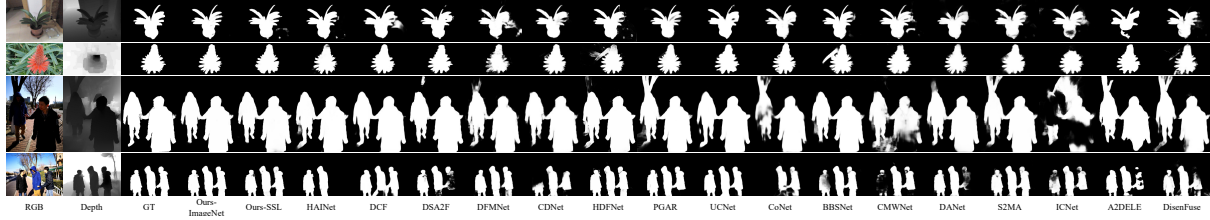


Figure 4: Visual comparison of different RGB-D SOD methods.

Model	F_{β}^{max}	F_{β}^w	S_m	E_m	\mathcal{M}
HAINet (Random Initialization)	0.875	0.793	0.857	0.896	0.064
HAINet (Load our SSL-P1 pretraining weight)	0.900	0.839	0.883	0.918	0.050
HAINet (Load ImageNet pretraining weight)	0.920	0.871	0.905	0.936	0.039
HDFNet (Random Initialization)	0.876	0.776	0.860	0.896	0.065
HDFNet (Load our SSL-P1 pretraining weight)	0.898	0.822	0.881	0.915	0.053
HDFNet (Load ImageNet pretraining weight)	0.916	0.860	0.901	0.934	0.040

Table 4: Evaluation of existing methods with different initialization in terms of Ave-Metric.

Model	F_{β}^{max}	F_{β}^w	S_m	E_m	\mathcal{M}	Ave - Rank
Random Initialization	0.879	0.792	0.868	0.904	0.062	17
NJUD + NLPR ~2,000	0.900	0.844	0.882	0.923	0.048	14
NJUD + NLPR + DUTLF-V2 (part) ~4,000	0.903	0.848	0.886	0.926	0.047	12
NJUD + NLPR + DUTLF-V2 ~6,000	0.906	0.855	0.890	0.929	0.045	9

Table 5: Evaluation of the SSL-based network with different number of pretraining examples in terms of Ave-Metric.

depth maps are close to the GT and the reconstructed RGB images clearly fit the semantics of the original images, such as the sky becomes blue and even the cat is colored with white. Next, we load the pretrained parameters from P1 to jointly train the second pretext (P2), depth-contour estimation. The visual results are shown in Fig. 6. Model 2 vs. Model 1 shows that the P1 task can significantly improve the representation capability of the two-stream encoder. Model 3 vs. Model 2, Model 5 vs. Model 4 and Model 7 vs. Model 6 demonstrate the effectiveness of the P2 task. In addition, Model 4 vs. Model 2 and Model 5 vs. Model 3 can further verify the effect of the CDA in the cross-modal fusion. While Model 6 vs. Model 2 and Model 7 vs. Model 3 show its benefits in the cross-level fusion. Finally, Model 9 vs. Model 8 indicates the overall contribution of two self-supervised learning pretexts. It can be seen that the performance is significantly improved with the gain of 7.95% and 27.42% in terms of the weighted F-measure and MAE, respectively. Besides, we load the pretraining weights of our proposed universal two-stream self-supervised encoder (SSL-P1) into the second and fourth methods (the third one is based on the ResNet-18 backbone) in Tab. 1 as the initialization and retrain them. In Tab. 4, we can see that using self-supervised pretraining weights can help two top-performing methods to consistently obtain a huge performance improvement compared to random initialization. This fully verifies the generalization ability of our SSL design. More comparisons can be found in the supplementary material.

Evaluation of The Scale of Pretraining Data. In Tab. 5, we list the performance of using different numbers of SSL training images. We successively add 2,185 training samples of NJUD and NLPR, 2,000 samples of DUFLF-V2 and the rest 2,207 ones of DUFLF-V2 to the training set. We train three SSL networks on $\sim 2,000 - \sim 6,000$ unlabeled samples, and then load their parameters to initialize the downstream network, respectively. We can see that when only $\sim 2,000$ samples are used, the SSL-based network al-

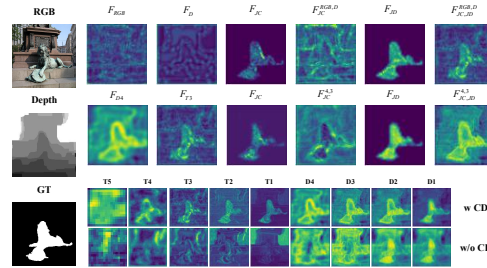


Figure 5: Illustration of the benefits of using the CDA. The first two rows correspond to different intermediate features in Fig. 2 in the cross-modal fusion and cross-level fusion, respectively. The third row shows visual comparison between the features of each level w and w/o CDA.

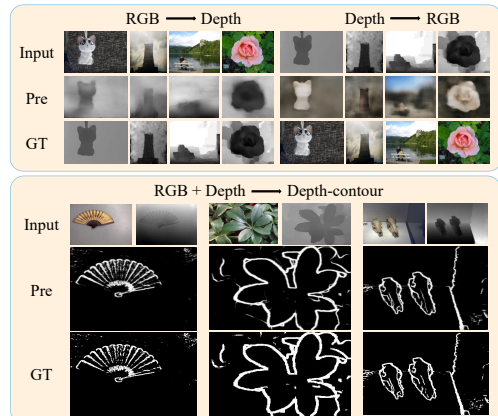


Figure 6: Visual results of the pretext tasks: cross-modal auto-encoder and depth-contour estimation.

ready significantly outperforms the randomly initialized network. With the increasing of training data, the performance is steadily improved, which shows that our SSL model has great potential. More comparisons can be found in the supplementary material.

Conclusion

In this work, we propose a novel self-supervised learning (SSL) scheme to accomplish effective pretraining for RGB-D SOD without requiring human annotation. The SSL pretext tasks contain cross-modal auto-encoder and depth-contour estimation, by which the network can capture rich context and reduce the gap between modalities. Besides, we design a consistency-difference aggregation module to combine cross-modal and cross-level information. Extensive experiments show our model performs well on RGB-D SOD datasets. As the first method of SSL in RGB-D SOD, it can be taken as a new baseline for future research.

Acknowledgement

This work was supported in part by the National Key RD Program of China #2018AAA0102001, the National Natural Science Foundation of China #61876202 and #61829102, the Dalian Science and Technology Innovation Foundation #2019J12GX039, the Liaoning Natural Science Foundation #2021-KF-12-10, and the Fundamental Research Funds for the Central Universities #DUT20ZD212.

References

- Achanta, R.; Hemami, S.; Estrada, F.; and Süsstrunk, S. 2009. Frequency-tuned salient region detection. In *CVPR*, 1597–1604.
- Agrawal, P.; Carreira, J.; and Malik, J. 2015. Learning to see by moving. In *ICCV*, 37–45.
- Ando, R. K.; and Zhang, T. 2005. A framework for learning predictive structures from multiple tasks and unlabeled data. *Journal of Machine Learning Research*, 6(Nov): 1817–1853.
- Caron, M.; Bojanowski, P.; Joulin, A.; and Douze, M. 2018. Deep clustering for unsupervised learning of visual features. In *ECCV*, 132–149.
- Chen, H.; Deng, Y.; Li, Y.; Hung, T.-Y.; and Lin, G. 2020. RGBD salient object detection via disentangled cross-modal fusion. *IEEE TIP*, 29: 8407–8416.
- Chen, S.; and Fu, Y. 2020. Progressively guided alternate refinement network for RGB-D salient object detection. In *ECCV*, 520–538.
- Cheng, Y.; Fu, H.; Wei, X.; Xiao, J.; and Cao, X. 2014. Depth enhanced saliency detection method. In *International Conference on Internet Multimedia Computing and Service*, 23.
- Collobert, R.; and Weston, J. 2008. A unified architecture for natural language processing: Deep neural networks with multitask learning. In *ICML*, 160–167.
- Deng, J.; Dong, W.; Socher, R.; Li, L.-J.; Li, K.; and Fei-Fei, L. 2009. Imagenet: A large-scale hierarchical image database. In *CVPR*, 248–255.
- Doersch, C.; Gupta, A.; and Efros, A. A. 2015. Unsupervised visual representation learning by context prediction. In *ICCV*, 1422–1430.
- Fan, D.-P.; Cheng, M.-M.; Liu, Y.; Li, T.; and Borji, A. 2017. Structure-measure: A new way to evaluate foreground maps. In *ICCV*, 4548–4557.
- Fan, D.-P.; Gong, C.; Cao, Y.; Ren, B.; Cheng, M.-M.; and Borji, A. 2018. Enhanced-alignment measure for binary foreground map evaluation. *arXiv preprint arXiv:1805.10421*.
- Fan, D.-P.; Ji, G.-P.; Zhou, T.; Chen, G.; Fu, H.; Shen, J.; and Shao, L. 2020a. Pranet: Parallel reverse attention network for polyp segmentation. In *MICCAI*, 263–273. Springer.
- Fan, D.-P.; Lin, Z.; Zhao, J.-X.; Liu, Y.; Zhang, Z.; Hou, Q.; Zhu, M.; and Cheng, M.-M. 2019. Rethinking RGB-D salient object detection: Models, datasets, and large-scale benchmarks. *arXiv preprint arXiv:1907.06781*.
- Fan, D.-P.; Zhai, Y.; Borji, A.; Yang, J.; and Shao, L. 2020b. BBS-Net: RGB-D salient object detection with a bifurcated backbone strategy network. In *ECCV*, 275–292.
- Fan, X.; Liu, Z.; and Sun, G. 2014. Salient region detection for stereoscopic images. In *International Conference on Digital Signal Processing*, 454–458.
- Feng, D.; Barnes, N.; You, S.; and McCarthy, C. 2016. Local background enclosure for RGB-D salient object detection. In *CVPR*, 2343–2350.
- Fu, K.; Fan, D.-P.; Ji, G.-P.; and Zhao, Q. 2020. Jl-dcf: Joint learning and densely-cooperative fusion framework for rgb-d salient object detection. In *CVPR*, 3052–3062.
- Goyal, P.; Mahajan, D.; Gupta, A.; and Misra, I. 2019. Scaling and benchmarking self-supervised visual representation learning. In *CVPR*, 6391–6400.
- Ji, W.; Li, J.; Yu, S.; Zhang, M.; Piao, Y.; Yao, S.; Bi, Q.; Ma, K.; Zheng, Y.; Lu, H.; et al. 2021a. Calibrated RGB-D Salient Object Detection. In *CVPR*, 9471–9481.
- Ji, W.; Li, J.; Zhang, M.; Piao, Y.; and Lu, H. 2020. Accurate rgb-d salient object detection via collaborative learning. In *ECCV*, 52–69.
- Ji, W.; Yu, S.; Wu, J.; Ma, K.; Bian, C.; Bi, Q.; Li, J.; Liu, H.; Cheng, L.; and Zheng, Y. 2021b. Learning Calibrated Medical Image Segmentation via Multi-Rater Agreement Modeling. In *CVPR*, 12341–12351.
- Jin, W.-D.; Xu, J.; Han, Q.; Zhang, Y.; and Cheng, M.-M. 2021. CDNet: Complementary Depth Network for RGB-D Salient Object Detection. *IEEE TIP*, 30: 3376–3390.
- Ju, R.; Ge, L.; Geng, W.; Ren, T.; and Wu, G. 2014. Depth saliency based on anisotropic center-surround difference. In *ICIP*, 1115–1119.
- Korbar, B.; Tran, D.; and Torresani, L. 2018. Cooperative learning of audio and video models from self-supervised synchronization. In *NeurIPS*, 7763–7774.
- Larsson, G.; Maire, M.; and Shakhnarovich, G. 2017. Colorization as a proxy task for visual understanding. In *CVPR*, 6874–6883.
- Li, D.; Li, R.; Wang, L.; Wang, Y.; Qi, J.; Zhang, L.; Liu, T.; Xu, Q.; and Lu, H. 2022. You Only Infer Once: Cross-Modal Meta-Transfer for Referring Video Object Segmentation. In *AAAI*.
- Li, G.; Liu, Z.; Chen, M.; Bai, Z.; Lin, W.; and Ling, H. 2021a. Hierarchical alternate interaction network for RGB-D salient object detection. *IEEE TIP*, 30: 3528–3542.
- Li, G.; Liu, Z.; and Ling, H. 2020. ICNet: Information Conversion Network for RGB-D Based Salient Object Detection. *IEEE TIP*, 29: 4873–4884.
- Li, G.; Liu, Z.; Ye, L.; Wang, Y.; and Ling, H. 2020. Cross-modal weighting network for rgb-d salient object detection. In *ECCV*, 665–681.
- Li, J.; Ji, W.; Bi, Q.; Yan, C.; Zhang, M.; Piao, Y.; Lu, H.; and Cheng, L. 2021b. Joint Semantic Mining for Weakly Supervised RGB-D Salient Object Detection. In *NeurIPS*.
- Lin, T.-Y.; Dollár, P.; Girshick, R.; He, K.; Hariharan, B.; and Belongie, S. 2017. Feature pyramid networks for object detection. In *CVPR*, 2117–2125.

- Liu, N.; Zhang, N.; and Han, J. 2020. Learning Selective Self-Mutual Attention for RGB-D Saliency Detection. In *CVPR*, 13756–13765.
- Liu, W.; Rabinovich, A.; and Berg, A. C. 2015. Parsenet: Looking wider to see better. *arXiv preprint arXiv:1506.04579*.
- Margolin, R.; Zelnik-Manor, L.; and Tal, A. 2014. How to evaluate foreground maps? In *CVPR*, 248–255.
- Mikolov, T.; Sutskever, I.; Chen, K.; Corrado, G. S.; and Dean, J. 2013. Distributed representations of words and phrases and their compositionality. In *NeurIPS*, 3111–3119.
- Misra, I.; Zitnick, C. L.; and Hebert, M. 2016. Shuffle and learn: unsupervised learning using temporal order verification. In *ECCV*, 527–544.
- Niu, Y.; Geng, Y.; Li, X.; and Liu, F. 2012. Leveraging stereopsis for saliency analysis. In *CVPR*, 454–461.
- Ocal, M.; and Mustafa, A. 2020. RealMonoDepth: Self-Supervised Monocular Depth Estimation for General Scenes. *arXiv preprint arXiv:2004.06267*.
- Okanohara, D.; and Tsujii, J. 2007. A discriminative language model with pseudo-negative samples. In *Proceedings of the 45th Annual Meeting of the Association of Computational Linguistics*, 73–80.
- Pang, Y.; Zhang, L.; Zhao, X.; and Lu, H. 2020a. Hierarchical dynamic filtering network for RGB-D salient object detection. In *ECCV*, 235–252.
- Pang, Y.; Zhao, X.; Zhang, L.; and Lu, H. 2020b. Multi-Scale Interactive Network for Salient Object Detection. In *CVPR*, 9413–9422.
- Pathak, D.; Krahenbuhl, P.; Donahue, J.; Darrell, T.; and Efros, A. A. 2016. Context encoders: Feature learning by inpainting. In *CVPR*, 2536–2544.
- Peng, H.; Li, B.; Xiong, W.; Hu, W.; and Ji, R. 2014. RGBD salient object detection: A benchmark and algorithms. In *ECCV*, 92–109.
- Piao, Y.; Ji, W.; Li, J.; Zhang, M.; and Lu, H. 2019. Depth-Induced Multi-Scale Recurrent Attention Network for Saliency Detection. In *ICCV*, 7254–7263.
- Piao, Y.; Rong, Z.; Xu, S.; Zhang, M.; and Lu, H. 2020a. DUT-LFSaliency: Versatile Dataset and Light Field-to-RGB Saliency Detection. *arXiv preprint arXiv:2012.15124*.
- Piao, Y.; Rong, Z.; Zhang, M.; Ren, W.; and Lu, H. 2020b. A2dele: Adaptive and Attentive Depth Distiller for Efficient RGB-D Salient Object Detection. In *CVPR*, 9060–9069.
- Pillai, S.; Ambrus, R.; and Gaidon, A. 2019. Superdepth: Self-supervised, super-resolved monocular depth estimation. 9250–9256.
- Ranftl, R.; Lasinger, K.; Hafner, D.; Schindler, K.; and Koltun, V. 2020. Towards robust monocular depth estimation: Mixing datasets for zero-shot cross-dataset transfer. *IEEE TPAMI*.
- Simonyan, K.; and Zisserman, A. 2014. Very deep convolutional networks for large-scale image recognition. *arXiv preprint arXiv:1409.1556*.
- Song, H.; Liu, Z.; Du, H.; Sun, G.; Le Meur, O.; and Ren, T. 2017. Depth-aware salient object detection and segmentation via multiscale discriminative saliency fusion and bootstrap learning. *IEEE TIP*, 26(9): 4204–4216.
- Sun, P.; Zhang, W.; Wang, H.; Li, S.; and Li, X. 2021. Deep RGB-D Saliency Detection with Depth-Sensitive Attention and Automatic Multi-Modal Fusion. In *CVPR*, 1407–1417.
- Wang, X.; and Gupta, A. 2015. Unsupervised learning of visual representations using videos. In *ICCV*, 2794–2802.
- Wang, Z.; Simoncelli, E. P.; and Bovik, A. C. 2003. Multi-scale structural similarity for image quality assessment. In *The Thirty-Seventh Asilomar Conference on Signals, Systems & Computers, 2003*, volume 2, 1398–1402.
- Wei, J.; Wang, S.; and Huang, Q. 2020. F3Net: Fusion, Feedback and Focus for Salient Object Detection. In *AAAI*.
- Zhang, J.; Fan, D.-P.; Dai, Y.; Anwar, S.; Saleh, F. S.; Zhang, T.; and Barnes, N. 2020a. UC-Net: Uncertainty inspired RGB-D saliency detection via conditional variational autoencoders. In *CVPR*, 8582–8591.
- Zhang, M.; Ji, W.; Piao, Y.; Li, J.; Zhang, Y.; Xu, S.; and Lu, H. 2020b. LFNet: Light field fusion network for salient object detection. *IEEE Transactions on Image Processing*, 29: 6276–6287.
- Zhang, M.; Li, J.; Ji, W.; Piao, Y.; and Lu, H. 2019. Memory-oriented Decoder for Light Field Salient Object Detection. In *NeurIPS*, 896–906.
- Zhang, M.; Liu, J.; Wang, Y.; Piao, Y.; Yao, S.; Ji, W.; Li, J.; Lu, H.; and Luo, Z. 2021a. Dynamic context-sensitive filtering network for video salient object detection. In *ICCV*, 1553–1563.
- Zhang, W.; Ji, G.-P.; Wang, Z.; Fu, K.; and Zhao, Q. 2021b. Depth Quality-Inspired Feature Manipulation for Efficient RGB-D Salient Object Detection. *arXiv preprint arXiv:2107.01779*.
- Zhao, J.-X.; Cao, Y.; Fan, D.-P.; Cheng, M.-M.; Li, X.-Y.; and Zhang, L. 2019. Contrast Prior and Fluid Pyramid Integration for RGBD Salient Object Detection. In *CVPR*.
- Zhao, X.; Pang, Y.; Yang, J.; Zhang, L.; and Lu, H. 2021. Multi-source fusion and automatic predictor selection for zero-shot video object segmentation. In *ACM MM*, 2645–2653.
- Zhao, X.; Pang, Y.; Zhang, L.; Lu, H.; and Zhang, L. 2020a. Suppress and balance: A simple gated network for salient object detection. In *ECCV*, 35–51.
- Zhao, X.; Zhang, L.; and Lu, H. 2021. Automatic Polyp Segmentation via Multi-scale Subtraction Network. In *MICCAI*. Springer.
- Zhao, X.; Zhang, L.; Pang, Y.; Lu, H.; and Zhang, L. 2020b. A single stream network for robust and real-time rgb-d salient object detection. In *ECCV*, 646–662.